RSC Advances

PAPER

View Article Online
View Journal | View Issue

Cite this: *RSC Adv.*, 2017, **7**, 31365

Facile synthesis of ZnO/CdS@ZIF-8 core–shell nanocomposites and their applications in photocatalytic degradation of organic dyes†

Rong-Mei Kong,[a] Yan Zhao,[a] Yiqun Zheng[b] and Fengli Qu *[a]

Zeolitic imidazolate frameworks (ZIF) are attracting considerable attention for their applications in adsorbents/separation as well as catalysis. In this article, we proposed a simple strategy to fabricate semiconductor–ZIF core–shell nanocomposites, which exhibited remarkable coherent function for adsorption and photocatalytic degradation of organic pollutants. The current nanocomposites were composed of ZnO/CdS and ZIF-8, where spindle-like ZnO nanoparticles not only acted as the seeding material but also worked as the Zn^{2+} source for the formation of ZIF-8. The as-prepared ZnO/CdS@ZIF-8 core–shell nanocomposites displayed distinct photocatalytic activity for methylene blue (MB) and rhodamine B (RhB) owing to the unique pore structure and thus absorption effect of the ZIF-8 shell. To this end, the ZnO/CdS@ZIF-8 core–shell nanocomposites could find important applications in photocatalytic degradation of pollutants.

Received 6th April 2017
Accepted 13th June 2017

DOI: 10.1039/c7ra03918b

rsc.li/rsc-advances

1. Introduction

Semiconductor-enabled photocatalytic degradation has been widely utilized as an effective approach to remove organic pollutants in waste water and effluents. Among those semiconductors, ZnO has been regarded as a promising candidate owing to its nontoxic and inexpensive characteristics, high thermal and chemical stability, and good electrical and optical properties.[1–7] However, the efficiency of photocurrent conversion of pristine ZnO is still limited because of the relatively optical band gap (*ca.* 3.37 eV) and high recombination rate of photogenerated electron–hole pairs.[8] To overcome these limitations, it has been expected that the introduction of a secondary semiconductor, including TiO_2,[9] CuO,[10] CdS,[11] CdSe,[12] among others, to form a ZnO-based hybrid semiconductor heterojunction can improve the photocatalytic activity of ZnO photocatalysts.[13] Take CdS as an example. CdS nanoparticles (NPs), an important II–IV semiconductor with a narrow but direct band gap (2.3 eV), which is effective for capturing visible light, have been intensively studied as popular visible light-active materials for photocatalysts[14–17] and photoelectrochemical sensors.[18,19] The problem of a high recombination rate of photogenerated electrons and holes of pure CdS NPs can be overcome by coupling CdS NPs with ZnO. When CdS NPs were anchored on the surface of ZnO, the photogenerated charge carriers could be effectively separated and transferred by a strong interfacial electric field owing to the well-matched overlapping band-structures.[20] So far, ZnO/CdS NPs have been explored as efficient visible-light photocatalysts for pollutant degradation and hydrogen production.[21–24]

Despite the success achieved in these demonstrations, it still remains a technical challenge to further improve the catalytic performance of ZnO/CdS. One possible solution would be the combination of ZnO/CdS with other functional materials to expect a synergetic effect. Recently, zeolitic imidazolate frameworks (ZIF) has attracted enormous research attention.[25] It has been known as a subclass of metal–organic frameworks, are crystalline tridimensional networks with well-defined porous structures consisting of metal ions or metal clusters bridged tetrahedral.[26] Compared with conventional inorganic porous materials, ZIF possess larger porosity and specific surface areas, and especially their pore size and surface functionality can be easily tuned upon selection of different metal ions and organic bridging ligands.[27] Consequently, much attention has been paid to potential applications of ZIF in sensors, catalysis, gas separation, and storage, where ZIF display strong molecule-size-selective ability due to the effect of the pore sizes.[28,29]

In the current work, we describe the fabrication of ZnO/CdS@ZIF-8 core–shell nanocomposites to enhance the intrinsic catalytic performance of ZnO/CdS semiconductor heterojunction.[30,31] The synthesis was conducted using CdS NPs-anchored spindle-like ZnO NPs as seeds to direct the heterogeneous growth of ZIF-8 and thus the formation of ZIF-8 shell. The synthetic strategy has three following advantages: (1)

[a]*College of Chemistry and Chemical Engineering, Qufu Normal University, Qufu 273165, Shandong, P. R. China. E-mail: fengliquhn@hotmail.com; Fax: +86 537 4456301; Tel: +86 537 4456301*

[b]*National Engineering Research Center for Colloidal Materials, Shandong University, Jinan 250000, Shandong, P. R. China*

† Electronic supplementary information (ESI) available. See DOI: 10.1039/c7ra03918b

ZnO/CdS seeds could serve as nucleation location for heterogeneous nucleation, which thus effectively eliminate the homogeneous nucleation and growth of ZIF materials that normally unavoided in the synthesis of ZIF-based core–shell product;[32,33] (2) ZnO in the seeds could provide Zn^{2+} during the formation of ZIF-8 and thus no more Zn precursor needs to be added in the growth step;[34,35] (3) unlike previous report using ZnO nanowire array as the starting material to fabricate semiconductor@ZIF core–shell structure,[36,37] the current work employs free-standing spindle-like ZnO/CdS NPs as seeds, which makes the catalyst much easier to suspend in the reaction system and interact with reactants. A set of characterizations, including SEM, TEM, EDS, XRD, and XPS were performed to study their size, shape, structure, and composition. Interestingly, the as-prepared ZnO/CdS@ZIF-8 exhibited excellent photocatalytic efficiency in degradation of methylene blue (MB) and rhodamine B (RhB) as model organic pollutants due to the synergetic function of semiconductor heterojunction and ZIF material.

2. Experimental section

2.1 Reagents and apparatus

Zinc nitrate hexahydrate ($Zn(NO_3)_2 \cdot 6H_2O$), sodium hydroxide (NaOH), ammonium fluoride (NH_4F) were purchased from Aladdin Industrial Inc. (Shanghai, China). Cadmium nitrate tetrahydrate ($Cd(NO_3)_2 \cdot 4H_2O$), thiourea, 2-methylimidazole, and methanol were obtained from Sigma-Aldrich Co. LLC. (St. Louis, USA). RhB and MB were purchased from Sinopharm Chemical Reagent Co. LTD. (Shanghai, China). All other reagents were used as received without further purification. All aqueous solutions were prepared with deionized water (resistivity > 18 MΩ cm) produced using a Millipore system.

2.2 Synthesis of spindle-like ZnO and ZnO/CdS NPs

In a typical synthesis of spindle-like ZnO NPs, 20 mL of $Zn(NO_3)_2 \cdot 6H_2O$ aqueous solution (5 mM) and 20 mL of NH_4F aqueous solution (20 mM) were mixed, followed by the dropwise addition of 10 mL of NaOH aqueous solution (20 mM) under stirring. A white precipitate was formed immediately and then partially dissolved upon further addition of NaOH. The solution became translucent and then turbid for 10 h under constant stirring at 50 °C. A white precipitate was collected by centrifugation and subsequently washed with ultrapure water and ethanol for several times, and finally dried at in an oven 60 °C in air overnight.

For the synthesis of ZnO/CdS NPs, 40 mg of the as-prepared spindle-like ZnO NPs was dispersed in 10 mL of ultrapure water containing 0.01 M of $Cd(NO_3)_2 \cdot 4H_2O$ and 0.01 M of thiourea under stirring. After the reaction was allowed to continue for 0.5 h, the orange ZnO/CdS product was obtained. The color change from white to orange suggested the successful formation and decoration of CdS NPs on the ZnO microspheres. The product was collected by centrifugation and washed with water for several times to remove dissolvable ionic impurities. The collected sample was dried in an oven at 80 °C in air for 6 h.

2.3 Preparation of ZnO/CdS@ZIF-8 core–shell nanocomposites

Typically, 50 mg of as-synthesized ZnO/CdS was introduced into 13.5 mL of 2-methylimidazole methanol solution (0.2 M). Then, the mixture was reacted at room temperature under stirring for 6 h. After centrifugation and washing with ethanol for three times, the products were dried in an oven at 60 °C overnight.

2.4 Photocatalytic degradation strategy

Photocatalytic performances were evaluated by photoreduction of RhB and MB in a single-component solution. The degradation experiments were carried out in open air and at room temperature.

Typically, 10 mg of ZnO/CdS@ZIF-8 catalyst was added into 100 mL of RhB or MB solution with a concentration of 8 mg L^{-1}. Prior to irradiation, the suspension was magnetically stirred in the dark for 60 min to reach adsorption equilibrium. During the photocatalysis, Xe lamp was used for visible light irradiation to the stirred suspension. Aliquots of sample (3 mL) were extracted at regular intervals for analysis. For comparison, ZnO/CdS nanocomposites were used as the control group. Every point in the photocatalytic curve was done twice to obtain average values. For each recycling test, the photocatalyst ZnO/CdS@ZIF-8 was collected by simple centrifugation and washed with deionized water for three times and dried. The concentrations of RhB and MB were measured using absorbance at 552 nm and 663 nm, respectively, in the UV-vis spectra according to Beer–Lambert law.

2.5 Characterization

The morphology and the size of the nanomaterials were collected on JSM-6700F electron microscope (SEM) equipped with an X-ray energy dispersive spectrometer (EDS) and a high-resolution transmission electron microscopy (HRTEM). The crystallinity and phase of the products were determined by an X-ray diffraction (XRD) MiniFlex600 (Rigaku Co. Japan) diffractometer. UV-vis extinction spectra were performed on a Varian Cary-300 bio UV/vis spectrophotometer (USA). X-ray photoelectron spectroscopy (XPS) was conducted onan ESCALAB 250Xi spectrometer (Thermo Fisher, USA). After pretreatment, nitrogen adsorption and desorption isothermal were measured at 77 K on a Quantachrome Instrument NOVA. A 300 W Xe lamp was used as the irradiation source with the light intensity of 300 μW cm^{-2} estimated by a radiometer (Ceaulight Corporation, China).

3. Results and discussion

3.1 Synthesis and characterization of ZnO/CdS@ZIF-8 core–shell nanocomposites

As shown in Fig. 1, in a typical synthetic procedure, the ZnO/CdS NPs were synthesized by mixing spindle-like ZnO NPs with precursors of Cd and S in aqueous solution *via* a facile synthesis. Then, the as-prepared ZnO/CdS NPs served as seeds to mix with 2-methylimidazole in methanol for 6 h at room temperature to allow the formation of ZIF-8 on the seed surface

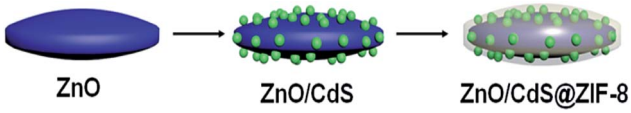

Fig. 1 Schematic illustrating the synthesis of ZnO/CdS@ZIF-8 core–shell nanocomposites.

to form ZnO/CdS@ZIF-8 core–shell nanocomposites. The morphology and microstructure of the as-prepared ZnO, ZnO/CdS, and ZnO/CdS@ZIF-8 were analyzed by SEM and TEM (Fig. 2). As shown in Fig. 2A, the SEM image showed that the ZnO NPs were uniform spindle-like structure with an average length of 400 nm. Fig. 2B displayed an SEM image of ZnO/CdS NPs, where CdS NPs were around 20 nm in diameter and uniformly distributed on the surface of ZnO NPs. The SEM image of ZnO/CdS@ZIF-8 showed in Fig. 2C displayed rougher surfaces than that of ZnO/CdS NPs, owing to the deposition of ZIF-8 shell on the ZnO/CdS NPs. Fig. 2D displayed the TEM image of ZnO/CdS NPs, which further demonstrated that the CdS NPs were uniformly distributed on the surface of ZnO NPs and the result consistent with the SEM image showed in Fig. 2B. The TEM image showed in Fig. 2E revealed the successful synthesis of ZnO/CdS@ZIF-8 core–shell nanocomposites, which was further confirmed by HRTEM given in Fig. 2F. It can be clearly seen that the ZIF-8 with a shell thickness of 4 nm was successfully deposited on the surface of ZnO/CdS NPs. The measured spacing of the crystallographic plane was 0.335 nm, which can be corresponded to the (111) lattice plane of a quadrilateral CdS crystal. The EDS spectrum (Fig. 2G) taken from the surface of ZnO/CdS@ZIF-8 exhibited the characteristic peaks of Zn, O, Cd, and S, which confirmed the elementary composition in the nanocomposite.

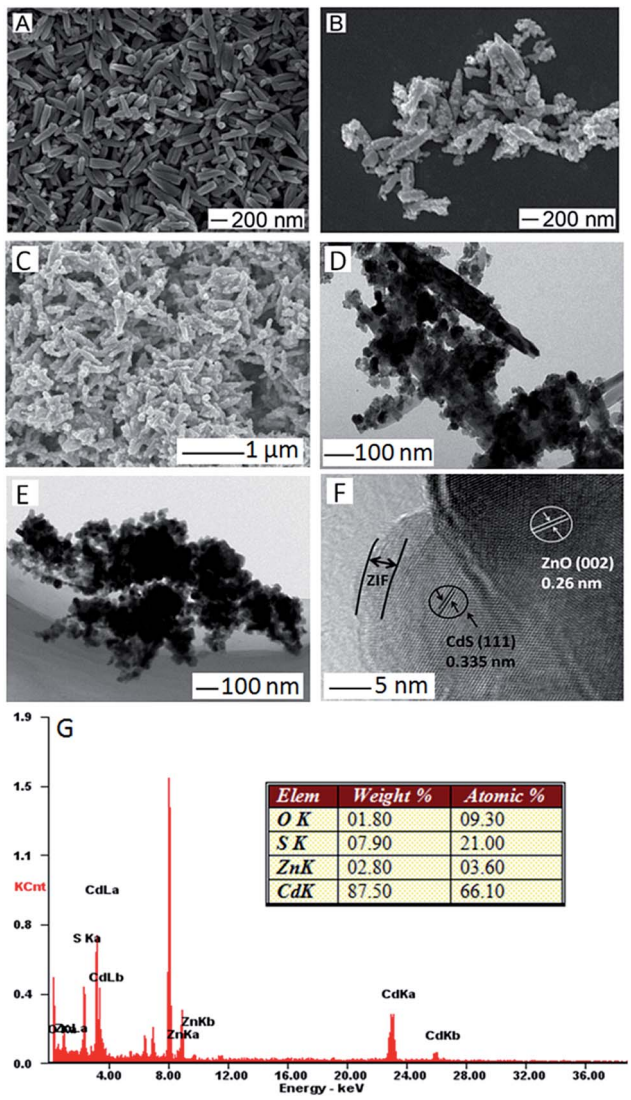

Fig. 2 SEM images of (A) ZnO, (B) ZnO/CdS, and (C) ZnO/CdS@ZIF-8, TEM images of (D) ZnO/CdS, and (E) ZnO/CdS@ZIF-8, (F) HRTEM images of ZnO/CdS@ZIF-8, (G) EDS spectrum of ZnO/CdS@ZIF-8 and the corresponding elements contents.

To investigate the overall crystallinity and crystal structures, the synthesized spindle-like ZnO, ZnO/CdS and ZnO/CdS@ZIF-8 were further identified by XRD. Fig. 3 showed the XRD patterns of the as-prepared ZnO, ZnO/CdS and ZnO/CdS@ZIF-8 nanocomposites with different main reflection peaks. For the XRD patterns of ZnO, the main reflection peaks could be matched to that of wurtzite structure of ZnO (JCPDS card no. 36-1451). No extra peak was detected by XRD, showing the purity of the sample. In comparison, the XRD patterns of ZnO/CdS exhibited new diffraction peaks, which can be indexed to the wurtzite CdS phase (JCPDS card no. 65-3414), confirming the presence of CdS. After the formation of ZIF-8 shell, the sample showed the same characteristic peaks with the simulated ZIF, in addition to those diffraction peaks assigned to ZnO/CdS. For example, the diffraction peak located at $2\theta = 7.3^{\circ}$ can be assigned to the (011) plane of ZIF-8.

The surface compositions and elemental analysis of ZnO/CdS@ZIF-8 were further investigated by XPS (Fig. S1†). Fig. S1A† presented the XPS spectrum of Zn 2p. The peak positions of Zn $2p_{1/2}$ and Zn $2p_{3/2}$ located at 1044.94 and 1021.84 eV. The O 1s and O–Zn group spectra of Fig. S1B† showed specific peaks centered at 533.59 and 533.43 eV,

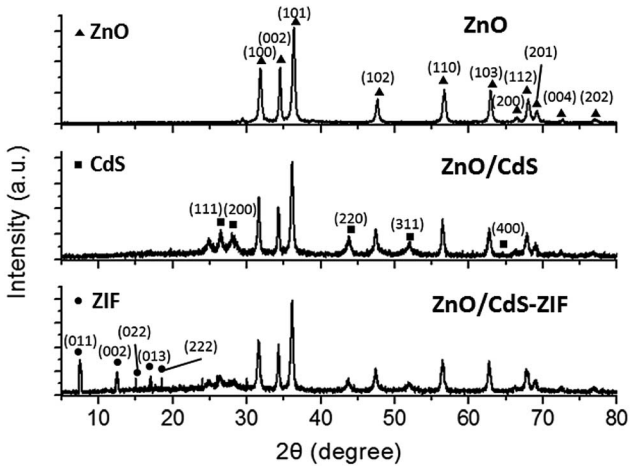

Fig. 3 XRD patterns of ZnO, ZnO/CdS and ZnO/CdS@ZIF-8.

respectively. The spectrum of Cd 3d in Fig. S1C† was subdivided into two separated peaks that correspond to Cd $3d_{3/2}$ (411.79 eV) and Cd $3d_{5/2}$ (405.09 eV) valence states. The spectrum of S 2p at 162.24 eV showed that the CdS NPs were well synthesized (Fig. S1D†). The binding energy at 405.44 eV in Fig. S1E† was attributable to N 1s. Additionally, the C 1s spectrum was shown in Fig. S1F,† the specific peak centered at 285.56 eV. The N 1s and C 1s peaks were attributed to the presence of ZIF-8 which was synthesized by 2-methylimidazole. Therefore, the XPS analysis confirmed the successful decoration of CdS NPs on the spindle-like ZnO NPs, and the formation of ZIF-8 shell on the surface of ZnO/CdS NPs, which was in accordance with the results of XRD analysis.

The nitrogen adsorption–desorption isotherms of ZnO/CdS and ZnO/CdS@ZIF-8 were shown in Fig. S2.† The curves for ZnO/CdS NPs (Fig. S2a†) were a type IV isotherm,[38] which shows low adsorption at low pressure and multilayer adsorption at high pressures owing to slits caused by assembly of ZnO/CdS NPs. The initial adsorption of ZnO/CdS@ZIF-8 was higher than that of ZnO/CdS (Fig. S2b†), indicating that micropores exist in ZnO/CdS@ZIF-8 nanocomposites,[38] which can be attributed to the frameworks of ZIF-8. The multilayer adsorption at high pressure corresponds to spherical morphology of the sample, similar to that of ZnO/CdS NPs. Therefore, for ZnO/CdS@ZIF-8, the higher adsorption ability of the ZIF shell played an important role in the improvement of the photocatalytic activity.

3.2 Photocatalytic degradation activity of ZnO/CdS@ZIF-8

To demonstrate the photocatalytic activity of the as-obtained ZnO/CdS@ZIF-8 nanocomposites for the degradation of organic pollutants, we carried out the model experiments for the photocatalytic degradation of MB and RhB under visible light irradiation, respectively. Prior to irradiation, the time period of ZnO/CdS@ZIF-8 nanocomposites for organic pollutants adsorption equilibrium was first investigated. The aqueous suspension of MB mixed with catalyst was magnetically stirred in the dark and corresponding UV-vis spectra were recorded. As shown in Fig. 4, the maximum absorbance of MB gradually decreased and no apparent change was observed after 60 min, indicating the adsorption reached equilibrium after 60 min. Therefore, adsorption time period of 60 min was chosen for the following photocatalytic degradation in this study.

The photodegradation of MB and RhB assisted by ZnO/CdS@ZIF-8 is shown in Fig. 5. For degradation of MB, after 120 min of irradiation, the characteristic absorbance peak of MB located at 663 nm undergoes a fairly large decrease and became considerably insignificant (Fig. 5A), indicating the complete consumption of MB in the system. For the RhB/ZnO/CdS@ZIF-8 system (Fig. 5C), the absorbance spectra of RhB showed two types of changes: one is a hypsochromic shift in the major absorbance peak; the other is a decrease in the peak intensity. The major absorbance peak of RhB shifts gradually from 552 to 540 nm and the intensity decreased from 1.6 to 0.6 after 120 min of irradiation. The final product with the absorbance peak located at 540 nm can be identified as an incompletely *N*-deethylated outcome of RhB, *N*,*N*,*N*′-triethyl rhodamine (TER), as reported by Watanabe and co-workers.[39] The results indicated that the as-synthesized ZnO/CdS@ZIF-8 core–shell nanocomposites exhibited good photocatalytic degradation activity for organic pollutants.

Pseudo-first-order rate kinetics with regard to the organic pollutant concentration could be used to evaluate the catalytic rate. The apparent rate constant k of ZnO/CdS@ZIF-8 for MB and RhB degradation calculated from the $\ln(C_t/C_0)$ *vs.* time plot, where C_t and C_0 correspond to the concentrations of MB and RhB at time t and 0, respectively. It could be calculated by the equation of $\ln(C_t/C_0) = kt$ that the kinetic constant k values of ZnO/CdS@ZIF-8 for MB (Fig. 5B, inset) and RhB (Fig. 5D, inset) were -0.031 min^{-1} and -0.018 min^{-1}, respectively. For comparison, the same photodegradation experiments of ZnO/CdS for MB and RhB were carried out, the corresponding kinetic constant k values were -0.021 and -0.009 min^{-1} (Fig. 6), respectively. The higher k value means a better photocatalytic activity, revealing that the ZnO/CdS@ZIF-8 nanocomposite has a better and higher catalytic efficiency for the adsorption and degradation of organic pollutant. The experimental results indicated that the improvement of photocatalytic activity of the ZnO/CdS@ZIF-8 could be ascribed to the ZIF shell. Since catalytic degradation being dependent on

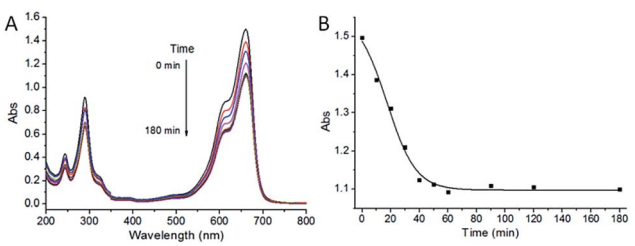

Fig. 4 The effect of adsorption time for the photocatalytic degradation of MB in the presence of ZnO/CdS@ZIF-8.

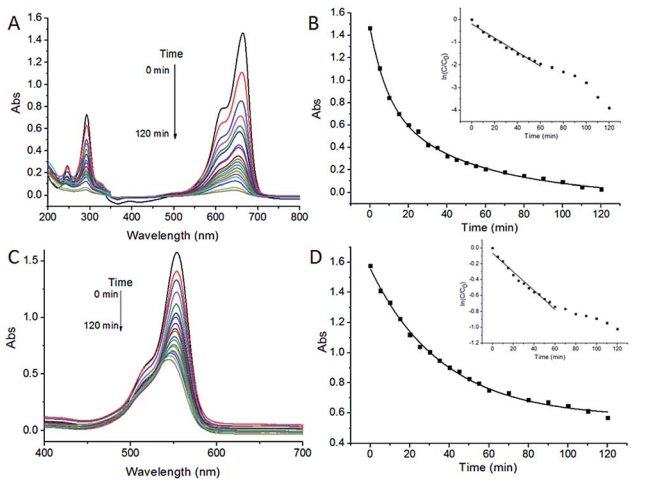

Fig. 5 UV-vis spectra showing time-dependent changes in characteristic absorbance of (A, B) MB and (C, D) RhB using ZnO/CdS@ZIF-8 as the catalyst. The inset in (B and D) show the corresponding plots of $\ln(C_t/C_0)$ *versus* time for the photocatalytic degradation of MB and RhB using ZnO/CdS@ZIF-8 as the catalyst.

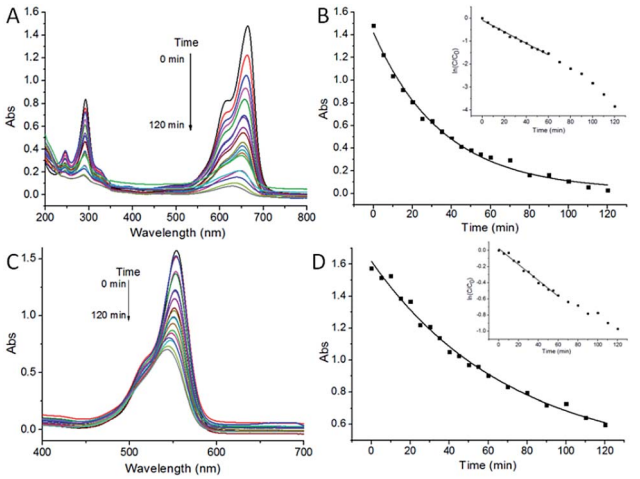

Fig. 6 UV-vis spectra showing time-dependent changes in characteristic absorbance of (A, B) MB and (C, D) RhB using ZnO/CdS as catalyst. The insets in (B and D) show the corresponding plots of $\ln(C_t/C_0)$ *versus* time for the photocatalytic degradation of MB and RhB using ZnO/CdS as catalyst.

accessibility of ZIF, the accelerated reaction kinetics of the organic pollutant was believed to result from the ZIF adsorption capability. Due to the adsorption effect of ZIF, pollutants rapidly gathered around the catalyst, leading to a relatively fast degradation rate.

The stability and reusability of target materials are another important standard for practical application. After adsorption experiments, adsorbents can be separated by simple centrifugation due to their insoluble properties in water. As shown in Fig. 7, in the four cyclic MB tests, the ZnO/CdS@ZIF-8 nanocomposites exhibited an excellent stability with an average MB removal efficiency, and no evident change has taken place for the photocatalytic activity, which indicated good photocatalytic stability of the ZnO/CdS@ZIF-8 nanocomposites. Similarly, the stability and reusability of the ZnO/CdS@ZIF-8 nanocomposites for the RhB photodegradation was investigated, and the results indicated that the excellent stability of ZnO/CdS@ZIF-8 for RhB removal efficiency (Fig. S3†).

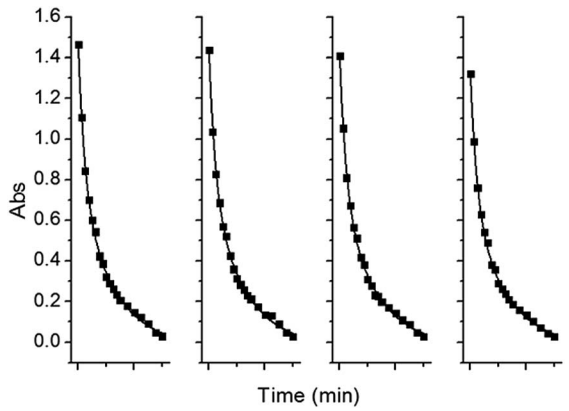

Fig. 7 Recyclability of the ZnO/CdS@ZIF-8 nanocomposites for the photocatalytic degradation of MB.

3.3 Photocatalytic degradation mechanism

The adsorption of organic pollutants onto the catalyst and the photoelectron transfer are both important factors for the performance of catalytic degradation of organic pollutants. Generally, photocatalysis is an oxidation process. The organic pollutants photodegradation occurs in the presence of semiconductor photocatalysts, an energetic light source, and an oxidizing agent such as oxygen or air.[40] The illumination of could generate oxidation species such as hydroxyl radicals ($^{\bullet}OH$), h^+ and superoxide radical ($^{\bullet}O^{2-}$) which have been reported as the active species in the degradation of pollutant molecules.[41]

To investigate the main oxidation species of ZnO/CdS@ZIF-8 nanocomposites, the different scavengers were introduced into the photocatalytic degradation reaction of MB and RhB, which to perform the relative roles of the reactive species and evaluate the photocatalytic mechanism of ZnO/CdS@ZIF-8. Here, the *p*-benzoquinone (BQ, 10 mM), disodium ethylenediaminetetraacetate (EDTA, 10 mM) and tertiary butanol (*t*-BuOH, 10 mM) were used as scavengers and added into the reaction system for trapping the specific reactive specie $^{\bullet}O^{2-}$, h^+, and $^{\bullet}OH$, respectively. As shown in Fig. S4A,† the degradation efficiency has a significant decrease for the photocatalytic degradation of MB when adding the *t*-BuOH for 120 min visible light irradiation, whereas BQ and EDTA with a slightly influences. It indicated that $^{\bullet}O^{2-}$ and $^{\bullet}OH$ were the main active species in the MB photocatalytic degradation process. For RhB photocatalytic degradation process, the degradation efficiency decreased obviously upon the addition of BQ and *t*-BuOH, while EDTA changed slightly. The result demonstrated that $^{\bullet}OH$ was the main active species in the RhB photocatalytic degradation process. The difference of the active species in the photocatalytic degradation process between MB and RhB may be due to their different energy gaps for electron transition.

According to the traditional theory about the photocatalytic degradation of organic pollutants and the above experimental results, a photocatalytic mechanism about ZnO/CdS@ZIF-8 nanocomposites was elucidated in Fig. 8. Firstly, the organic pollutant molecules are were captured by ZIF onto the ZnO/CdS composites surface where the photocatalytic reaction takes place. It is well accepted that the organic pollutants can be captured by ZIF *via* three mechanisms: (1) binding to the open metal sites on ZIF; (2) interacting with the functional groups on ZIF; (3) electrostatic interactions with ZIF. The basis of constructing such an unusual nanocomposite was the electrostatic adsorption of Cd based complex ions on the polar surfaces of ZnO substrate. The presence of photoanode in ZnO/CdS nanocomposite significantly improved the photochemical property. The position of CdS and ZnO bands had type-II alignment where the conduction band (CB) edge of ZnO was located between the CB and the valence band (VB) of CdS. In this configuration, when the electron–hole pairs were generated by visible-light excitation in CdS nanoparticles, the photoelectrons could be transferred to the CB of ZnO, which facilitated the charge separation process of the electron–hole pairs before they recombined. Thus, the photocorrosion induced by oxidation

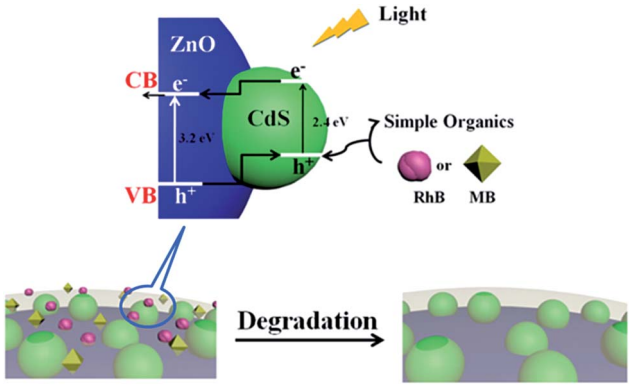

Fig. 8 Schematic of the photocatalytic degradation mechanism for MB and RhB.

could be effectively suppressed by rapid reaction rate. The valence band holes capture hydroxide ions (OH^-) or water (H_2O) to form the extremely powerful, non-selective, oxidising $^{\bullet}OH$. The enriched electrons on the CdS could combine with oxygen (O_2) in the solution to form $^{\bullet}O^{2-}$. The generated $^{\bullet}OH$ and $^{\bullet}O^{2-}$ played important role in the photodegradation process, leading to dramatic photocatalytic performance.

4. Conclusions

In summary, we have successfully synthesized ZnO/CdS@ZIF-8 core–shell nanocomposites and investigated their photocatalytic performance in degradation of organic dyes. The spindle-like ZnO not only acted as the nucleation core but also provided Zn^{2+} for the formation of ZIF-8. Various characterizations, including SEM, TEM, EDS, XRD, and XPS, have been performed to confirm their shape, structure, and composition. Compared to pure ZnO/CdS, the presence of ZIF-8 shell in the ZnO/CdS@ZIF-8 contributed significantly to the enhanced photocatalytic performance in degradation of RhB and MB. Owing to the unique pore structure and absorption capability of ZIF-8, it became much easier for organic molecules to diffuse and interact on the catalyst surface. In particular, when ZnO/CdS@ZIF-8 was used as the catalyst, the rate constant of photocatalytic degradation of MB and RhB achieved $-0.031\ min^{-1}$ and $-0.018\ min^{-1}$, respectively, as compared to that of the reaction using ZnO/CdS as the catalyst (rate constant: $-0.021\ min^{-1}$ and $-0.009\ min^{-1}$ for photocatalytic degradation of MB and RhB, respectively). The synergetic effect proposed in the current report takes advantages of both ZIF and semiconductor materials and could be potentially extended to similar catalytic applications.

Acknowledgements

This work was supported by the National Natural Science Foundation of China (21375076), Key Research and Development Program of Shandong Province (2015GSF121031), and the Project of University-industry Cooperation of Jining City (2014018).

References

1 X.-G. Han, H.-Z. He, Q. Kuang, X. Zhou, X.-H. Zhang, T. Xu, Z.-X. Xie and L.-S. Zheng, *J. Phys. Chem. C*, 2009, **113**, 584–589.
2 J. Xu, J. Han, Y. Zhang, Y. A. Sun and B. Xie, *Sens. Actuators, B*, 2008, **132**, 334–339.
3 X. Wang, C. J. Summers and Z. L. Wang, *Nano Lett.*, 2004, **4**, 423–426.
4 M. H. Huang, S. Mao, H. Feick, H. Yan, Y. Wu, H. Kind, E. Weber, R. Russo and P. Yang, *Science*, 2001, **292**, 1897.
5 H. Tang, M. Yan, X. Ma, H. Zhang, M. Wang and D. Yang, *Sens. Actuators, B*, 2006, **113**, 324–328.
6 C. Hariharan, *Appl. Catal., A*, 2006, **304**, 55–61.
7 Z. L. Wang, *Appl. Phys. A*, 2007, **88**, 7–15.
8 Ü. Özgür, Y. I. Alivov, C. Liu, A. Teke, M. A. Reshchikov, S. Doğan, V. Avrutin, S. J. Cho and H. Morkoç, *J. Appl. Phys.*, 2005, **98**, 041301.
9 F. X. Xiao, *ACS Appl. Mater. Interfaces*, 2016, **4**, 7055–7063.
10 R. Saravanan, S. Karthikeyan, V. K. Gupta, G. Sekaran, V. Narayanan and A. Stephen, *Mater. Sci. Eng., C*, 2013, **33**, 91–98.
11 X. Wang, G. Liu, Z. G. Chen, F. Li, L. Wang, G. Q. Lu and H. M. Cheng, *Chem. Commun.*, 2009, 3452–3454.
12 C. Eley, T. Li, F. Liao, S. M. Fairclough, J. M. Smith, G. Smith and S. C. E. Tsang, *Angew. Chem., Int. Ed.*, 2014, **53**, 7838–7842.
13 S. Sakthivel, S. U. Geissen, D. W. Bahnemann, V. Murugesan and A. Vogelpohl, *J. Photochem. Photobiol., A*, 2002, **148**, 283–293.
14 T. Jia, A. Kolpin, C. Ma, R. C.-T. Chan, W.-M. Kwok and S. C. E. Tsang, *Chem. Commun.*, 2014, **50**, 1185–1188.
15 X. Pan and Y.-J. Xu, *J. Phys. Chem. C*, 2015, **119**, 7184–7194.
16 L. J. Zhang, R. Zheng, S. Li, B. K. Liu, D. J. Wang, L. L. Wang and T. F. Xie, *ACS Appl. Mater. Interfaces*, 2014, **6**, 13406–13412.
17 Q. Xiang, F. Cheng and D. Lang, *ChemSusChem*, 2016, **9**, 996–1002.
18 Z. A. Peng and X. Peng, *J. Am. Chem. Soc.*, 2001, **123**, 183–184.
19 R. Vogel, P. Hoyer and H. Weller, *J. Phys. Chem.*, 1994, **98**, 3183–3188.
20 M. Ding, N. Yao, C. Wang, J. Huang, M. Shao, S. Zhang, P. Li, X. Deng and X. Xu, *Nanoscale Res. Lett.*, 2016, **11**, 1–7.
21 F. Xu, Y. Yuan, H. Han, D. Wu, Z. Gao and K. Jiang, *CrystEngComm*, 2012, **14**, 3615–3622.
22 P. Kundu, P. A. Deshpande, G. Madras and N. Ravishankar, *J. Mater. Chem.*, 2011, **21**, 4209–4216.
23 S. Khanchandani, S. Kundu, A. Patra and A. K. Ganguli, *J. Phys. Chem. C*, 2012, **116**, 23653–23662.
24 B. Li and Y. Wang, *J. Phys. Chem. Solids*, 2011, **72**, 1165–1169.
25 R. Banerjee, A. Phan, B. Wang, C. Knobler, H. Furukawa, M. O'Keeffe and O. M. Yaghi, *Science*, 2008, **319**, 939–943.
26 O. M. Yaghi, G. Li and H. Li, *Nature*, 1995, **378**, 703–706.
27 N. Chang, Z. Y. Gu and X. P. Yan, *J. Am. Chem. Soc.*, 2010, **132**, 13645–13647.

28 A. Phan, C. J. Doonan, F. J. Uriberomo, C. B. Knobler, M. O'Keeffe and O. M. Yaghi, *Acc. Chem. Res.*, 2016, **43**, 58–67.
29 J. Cravillon, S. Münzer, S. J. Lohmeier, A. Feldhoff, K. Huber and M. Wiebcke, *Chem. Mater.*, 2009, **21**, 1410–1412.
30 J. Zheng, C. Cheng, W. J. Fang, C. Chen, R. W. Yan, H. X. Huai and C. C. Wang, *CrystEngComm*, 2014, **16**, 3960–3964.
31 M. Zeng, Z. Chai, X. Deng, Q. Li, S. Feng, J. Wang and D. Xu, *Nano Res.*, 2016, 1–6.
32 F. Ke, L.-G. Qiu, Y.-P. Yuan, X. Jiang and J.-F. Zhu, *J. Mater. Chem.*, 2012, **22**, 9497–9500.
33 N. Liu, Y. Yao, J. J. Cha, M. T. McDowell, Y. Han and Y. Cui, *Nano Res.*, 2012, **5**, 109–116.
34 Y. Sun, Q. Zhang, X. Xu, L. Zhang, Z. Wu, J. Guo and G. Lu, *Eur. J. Inorg. Chem.*, 2016, **22**, 3553–3558.
35 E. Zanchetta, L. Malfatti, R. Ricco, M. J. Styles, F. Lisi, C. J. Coghlan, C. J. Doonan, A. J. Hill, G. Brusatin and P. Falcaro, *Chem. Mater.*, 2014, **27**, 690.
36 W. W. Zhan, Q. Kuang, J. Z. Zhou, X. J. Kong, Z. X. Xie and L. S. Zheng, *J. Am. Chem. Soc.*, 2013, **135**, 1926–1933.
37 J. L. Yang, S. J. An, W. I. Park, G. C. Yi and W. Choi, *Adv. Mater.*, 2004, **16**, 1661–1664.
38 M. Kruk and M. Jaroniec, *Chem. Mater.*, 2001, **13**, 3169–3183.
39 T. Watanabe, T. Takizawa and K. Honda, *J. Phys. Chem.*, 1977, **81**, 1845–1851.
40 S. Xiao, L. Zhao and J. Lian, *Catal. Lett.*, 2014, **144**, 347–354.
41 S. Khanchandani, S. Kundu, A. Patra and A. K. Ganguli, *J. Phys. Chem. C*, 2013, **117**, 5558–5567.